Chapter 8

Terahertz Waveform Measurements Using a Chirped Optical Pulse and Terahertz Spectroscopy of Reverse Micellar Solution: Towards Time-resolved Terahertz Spectroscopy of Protein in Water

Hiroshi Murakami

Additional information is available at the end of the chapter

http://dx.doi.org/10.5772/67195

Abstract

One challenging research target using terahertz spectroscopy is time-resolved terahertz spectroscopy of protein molecules to clarify the relationship between protein's functions and the low-frequency collective motion within the molecule. Our results on two research topics necessary for this target are described. One is single-shot measurements of terahertz waveform that has large advantages in time-resolved terahertz spectroscopy. We examined experimentally and theoretically single-shot measurements using chirped optical pulses. The other is terahertz spectroscopy of reverse micellar solutions in which nanometer-sized water droplets are formed. Protein powder is usually used as a sample for terahertz spectroscopy because the absorption of terahertz waves by solvent water is very strong in aqueous solutions of protein, although protein molecules work in water. The absorption of terahertz waves by the nonpolar oil solvent in reverse micellar solution is considerably weak compared with that by water. We demonstrated that terahertz absorption spectra of protein in liquids are obtained by the use of protein-containing reverse micellar solution. On the other hand, a nanometer-sized water droplet in reverse micellar solutions is a promising candidate for studies of supercooled water. We made temperature-dependent terahertz spectroscopy of the water droplet to study collective water motions due to hydrogen bond networks.

Keywords: terahertz spectroscopy, time-resolved, single-shot measurement, biomolecules, reverse micelle, water, chirped pulse, nanoconfinement, temperature dependence

1. Introduction

1.1. Terahertz time-domain spectroscopy

At present, terahertz time-domain spectroscopy (THz-TDS) using a femtosecond laser is a popular method to measure the optical constant of materials in the terahertz frequency range, and its applications for medical science and industry are being investigated [1, 2]. A schematic diagram of THz-TDS using two photoconductive antennas is depicted in **Figure 1(a)**. A femtosecond laser pulse is divided into two beams. One is used to generate a terahertz electromagnetic wave by accelerating photoelectrons due to ultrafast laser irradiation onto the DC-biased photoconductive antenna. The other is used to obtain the temporal waveform of the terahertz electronic field that biases the other photoconductive antenna, where the photocurrent induced by the laser pulse is proportional to the amplitude of the electric field and is measured with a lock-in amplifier. The terahertz wave exhibits roughly a picosecond monocyclic pulse (**Figure 1(b)**) and a very small part of its waveform can be sampled by the femtosecond probe pulse. The temporal overlapping between the two pulses is sequentially varied by use of an optical delay line, and the whole terahertz waveform is obtained. The temporal waveform of the terahertz field pulse transmitted through a sample material is converted to the spectrum in the frequency domain by the Fourier transform (**Figure 1(c)**) and then the optical constant of the material is derived using the spectrum obtained in the same way from the terahertz field pulse transmitted through a reference material (e.g., solvent liquid for a solution sample). One excellent advantage of this method is to obtain the complex permittivity (or refractive index) of materials directly from the measurement because one measures the electric field amplitude, and not the intensity, as seen in **Figure 1(b)**.

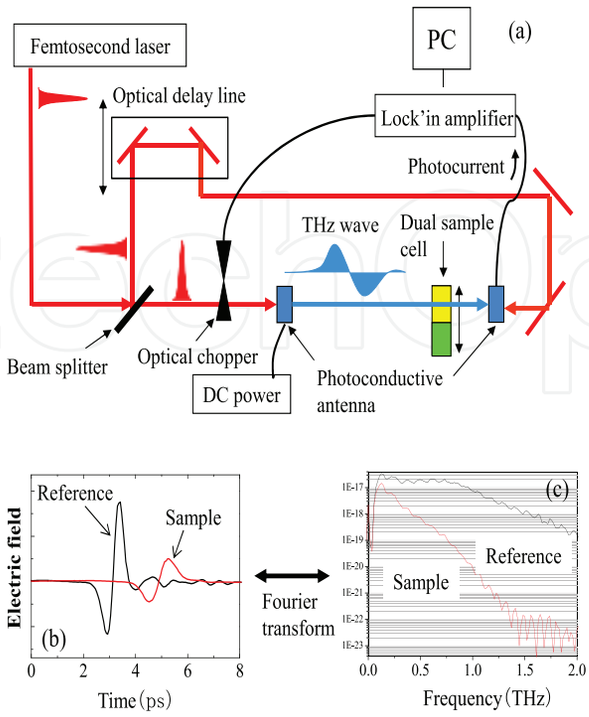

Figure 1. (a) Schematic diagram of terahertz time-domain spectroscopy (THz-TDS). (b) Terahertz waveforms after transmission through reference and sample solutions. (c) Frequency spectra obtained from the Fourier transform of the terahertz waveforms.

http://dx.doi.org/10.5772/67195

1.2. Optical-pump terahertz-probe time-resolved terahertz spectroscopy

The next step of THz-TDS is optical-pump terahertz-probe (OPTP) spectroscopy using pulsed terahertz waves; that is, one examines the time-dependent complex permittivity of materials in the terahertz frequency range after abrupt change in the electronic state of the material induced by an optical laser pulse [3–5]. Further, an enhancement in the peak intensity of the terahertz pulse wave has opened up terahertz-pump terahertz-probe spectroscopy and nonlinear terahertz spectroscopy [6–8]. These time-resolved terahertz spectroscopies have been performed largely for solids such as semiconductor and graphene. OPTP spectroscopy requires two optical delay-line systems if THz-TDS is employed for the terahertz wave probe; one is used for THz-TDS, and the other controls the time difference between the optical and terahertz pulses at the material. One issue of this OPTP spectroscopy is that it is difficult to apply it to sample materials that undergo an irreversible process or show a relaxation process with a time constant longer than the period of pulse repetition of the femtosecond laser because the terahertz waveform measured using THz-TDS is deformed. One method to overcome this issue is a single-shot measurement of terahertz waveforms; accordingly, this measurement needs only one optical delay-line system for control of pump-probe delay time.

1.3. Single-shot measurements of terahertz waveforms using a chirped optical pulse

Single-shot measurements of a terahertz waveform can be achieved by a combination of electro-optic detection using a chirped optical pulse (EODCP) and measurements of the chirped pulse with a spectrometer. This was first proposed and accomplished by Jiang and Zhang [9]. The result was discussed on the basis of a theoretical expression approximately derived [10]. We examined the method in detail as functions of the chirp rate and spectral resolution of the spectrometer and analyzed the experimental results using the theoretical expression analytically derived [11]. Moreover, on the basis of EODCP, we measured the complex refractive index of a material in the terahertz range and conducted OPTP spectroscopy. These results show that this method is applicable to terahertz spectroscopy and a promising method for OPTP spectroscopy. These results are described in Section 2.

1.4. Relationship between terahertz collective motions within a protein molecule and its function

Biomolecules, such as protein and DNA, play a fundamental role in the biological function of living cells. Further, it is believed that low-frequency collective motions in a protein molecule in the terahertz range play an important role in protein's functions [12–15]. Hence, terahertz spectroscopy of biomolecules has been extensively conducted [16–21]. Moreover, OPTP spectroscopy allows us to observe the collective motions during the protein function. Time-dependent change in the terahertz motions of a protein is measured after an optical pulse initiates a chemical reaction in the molecule, such as enzyme reaction and protein folding, by OPTP spectroscopy. If a specific collective motion is involved in the reaction, spectral change is expected to be observed at the frequency characteristic of the collective motion. However, there is a serious issue for terahertz spectroscopy of proteins. Although proteins work in water, protein powders are usually used as a sample for terahertz spectroscopy because absorption of terahertz wave by solvent water is very strong in aqueous solutions of

protein and because it is difficult to obtain the terahertz signal due to the protein molecule. To overcome this problem, we employ reverse micelles.

1.5. Reverse micelle

A reverse micelle is formed by self-assembly of surfactant molecules in a nonpolar oil solvent and becomes a nanometer-scale spherical cage filled with water, as shown in **Figure 2** [22, 23]. The size of reverse micelles can be experimentally controlled by the water-surfactant molar ratio (w_0). Water-soluble molecules, such as proteins and DNA, can be dissolved in the reverse micelle. Because absorption of terahertz waves by nonpolar solvents is considerably weak compared with polar solvents such as water, the absorption background signal due to the solvent was very low for reverse micellar solutions. We demonstrated that terahertz signal due to protein molecules is obtained by use of protein-containing reverse (PCR) micellar solution [24], as described in Section 4.

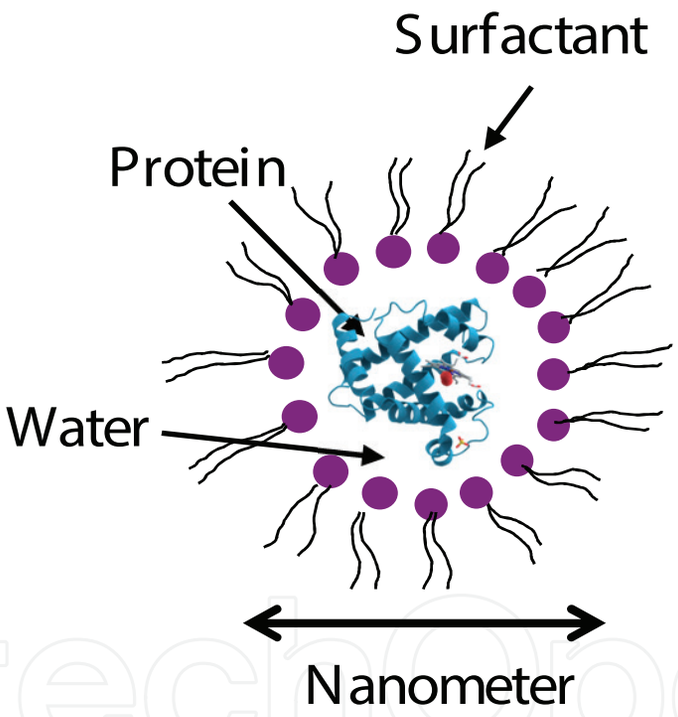

Figure 2. Schematic cross-section of a protein-containing reverse micelle.

A reverse micelle is a potential candidate for studying biomolecules and their surrounding waters under the condition similar to those in living cells. Cells are crowded with many kinds of molecules, and so the surroundings of biomolecules are different from those in the dilute aqueous solution. This is referred to as a macromolecular crowding effect [25, 26]. Therefore, the effect needs to be studied to clarify biomolecular function. In particular, the difference in the state of the surrounding waters of biomolecules will have a significant effect on their function [27, 28]. Nevertheless, biomolecules are usually studied in the dilute aqueous solutions.

http://dx.doi.org/10.5772/67195

1.6. Terahertz spectroscopy of nanoconfined water for studies on thermodynamic anomaly of water at 228 K

Water has the density maximum at 4°C. This is a well-known anomalous property of water, which is responsible for the fact that ice floats on the top of liquid water. Further, most thermodynamic properties of supercooled water display strong anomalies, for example, the isobaric specific heat and thermal expansion appear to diverge at 228 K [29]. Since the discovery of the anomalies, much attention has been paid to the properties of supercooled water. Several hypotheses, such as the liquid-liquid phase transition hypothesis, were proposed for a unified understanding of water [30, 31]. As for the experimental studies of supercooled water, it is necessary to use mesoporous materials such as MCM-41 because water confined in such materials does not freeze far below the melting point [32–35]. However, the interaction between confined water and the internal surface of the cage used for the confinement could affect the properties of water [31]. This is a serious issue for supercooled water studies.

A reverse micelle is a promising candidate for studies of supercooled water distinguished from the mesoporous material by the following reasons. Reverse micelles in liquids will provide soft confinement compared with the nanopore in solid materials. Further, we have recently shown by use of a molecular probe introduced into reverse micelles that water shedding from reverse micelles with an aqueous cavity radius of ~1 nm occurs below the melting point of water and that the water droplets extracted are dispersed in the solution down to the melting point of the oil solvent (~170 K) [36]. This indicates that it is possible to make temperature-dependent measurements of nanometer-sized water droplets over a wide temperature range. Moreover, the water shedding allows us to use a nanometer-sized water droplet free from the cage.

There are studies on the temperature-dependent properties of confined-water using reverse micelles [37–40], but terahertz spectroscopy has never been applied to it. Terahertz spectroscopy is well suited for studying cooperative motions of water due to the hydrogen bond network on time scales of picoseconds [41–44]. It is believed that the hydrogen bond network is a key to elucidate the anomalous properties of water. From terahertz spectroscopy of water above the melting point, Rønne and coworkers suggested that the relaxation time appears to diverge at ~228 K as the temperature is decreased [41, 42]. This implies that terahertz spectroscopy of water can provide information on the microscopic mechanism underlying the thermodynamic anomaly of water at low temperatures. The result of terahertz spectroscopy of water in reverse micellar solutions as a function of temperature is presented in Section 5 [45].

2. Terahertz waveform measurements using EODCP

2.1. EODCP

In THz-TDS using electro-optic (EO) detection, the detector module in **Figure 1(a)** consists of an EO crystal such as ZnTe, which is put between the two polarizers, and a photodiode for measurements of the probe laser intensity. The probe pulse is overlapped with the terahertz field pulse within the crystal, and the magnitude of the Pockels effect proportional to the

amplitude of the terahertz field is obtained from measurements of the intensity of the probe pulse subject to the birefringence in the crossed-polarizers configuration.

The method using EODCP is schematically described in **Figure 3**. A femtosecond probe pulse is linearly chirped and temporally broadened to cover the terahertz waveform examined. The chirped probe pulse is overlapped with a terahertz field pulse within the EO crystal, modulated by the terahertz field, and dispersed onto a multichannel detector combined with a spectrometer. Since the wavelength axis can be converted to the time axis using the value of the chirp rate, the terahertz field waveform is derived from the two spectra of the probe pulses with and without terahertz field modulation. Thus, a single-shot measurement of the terahertz waveform is made using EODCP. Jiang and Zhang used a chirped pulse with a temporal width of ~30 ps and obtained a terahertz waveform three times broader than the original pulse width measured by THz-TDS with delay scanning using an unchirped probe pulse [9]. Further, Sun and coworkers analyzed the dependence of the EODCP-derived terahertz waveform on the chirp rate by assuming that the stationary phase method is applicable [10]. The EODCP-derived terahertz waveform is monocyclic for a monocyclic original terahertz field as long as the stationary phase method is used. On the other hand, the EODCP-derived terahertz waveform changes with the chirp rate and the spectral resolution of the spectrometer, and hence one requires an analytical expression of the EODCP-derived terahertz waveform without such an assumption for analysis of a variety of terahertz waveforms.

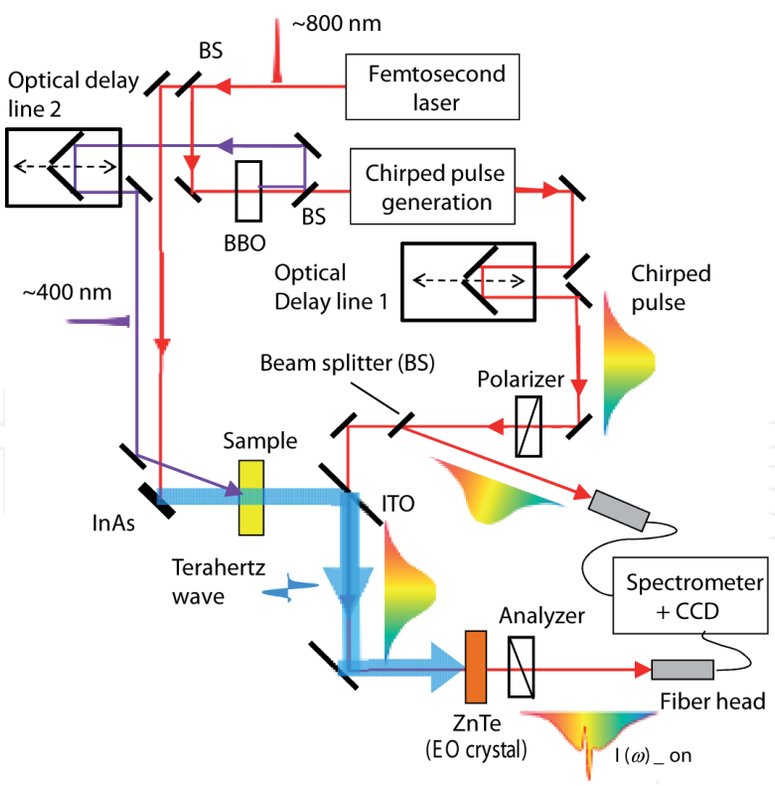

Figure 3. Schematic diagram of the experimental setup for time-resolved terahertz spectroscopy with electro-optic detection using a chirped probe pulse (EODCP) of the terahertz wave. A double-beam configuration was employed to obtain the chirped probe pulses with modulation due to the terahertz field and without it simultaneously. ITO is indium tin oxide.

http://dx.doi.org/10.5772/67195

2.2. Expression of the EODCP-derived terahertz waveform

We derive an expression of the EODCP-derived terahertz field waveform in this section. Denoting the electric field waveform of a chirped probe pulse by $C(t)$, we give the temporal shape of the chirped pulse modulated by a terahertz field $E_{THz}(t)$ as follows:

$$M(t) = C(t)\left[b + k\,E_{THz}(t-\tau)\right], \tag{1}$$

where k is a modulation coefficient, τ is the delay time between the terahertz field pulse and the chirped pulse, and b is the transmission coefficient because the probe pulse passes partly through the two crossed polarizers, e.g., owing to the inherent residual birefringence of the EO crystal or the finite extinction ratio of the polarizers. By comparing the EODCP-derived terahertz waveform with numerical results, Yellampalle and coworkers [46] showed that Eq. (1) is valid for an EO crystal with sufficient residual birefringence, as in the present study using a 1-mm-thick ZnTe crystal.

The waveform of the chirped pulse is defined as $C(t) = \exp(-t^2 T_c^{-2} - iat^2 - i\omega_0 t)$, where T_c, $2a$, and ω_0 are the width, chirp rate, and central frequency of the pulse, respectively. We give a monocyclic original terahertz field waveform by $E_{THz}(t) = \frac{t}{\Delta T}\exp(-t^2/\Delta T^2)$, which is a symmetrically bipolar function and represents a global feature of the terahertz field waveform generated by a femtosecond laser. If the modulated probe pulse is measured with a spectrometer with a multichannel detector, the spectral intensity $I(\omega)\_on$ is expressed by

$$I(\omega)\_\text{on} \propto \int_{-\infty}^{\infty} g(\omega-\omega')\left|\int_{-\infty}^{\infty} M(t)\exp(i\omega' t)dt\right|^2 d\omega', \tag{2}$$

where $g(\omega-\omega')$ is the spectral response function of the spectrometer; we set $g(\omega-\omega') = \delta(\omega-\omega')$ in this derivation. One can solve Eq. (2) by using Gaussian integrals and dealing with complex numbers in the polar form. We follow the procedure of Jiang and Zhang to derive the terahertz waveform from EODCP [9], namely,

$$E_{mes}(\omega) = \frac{I(\omega)\_\text{on} - I(\omega)\_\text{off}}{I(\omega)\_\text{off}}, \tag{3}$$

where $I(\omega)\_off$ is obtained by putting $M(t) = b\,C(t)$ in Eq. (2). Finally, we obtain an expression of the terahertz waveform as

$$\begin{aligned} E_{mes}(\omega) \propto & -\left\{\frac{2\tau}{T_c^2}\cos[\theta(\Delta\omega)] - (\Delta\omega + 2a\tau)\sin[\theta(\Delta\omega)]\right\} \\ & \times \exp\left[-\frac{\Delta\omega^2}{4}\left(\frac{1}{\beta + a^2\beta^{-1}} - \frac{1}{T_c^2\gamma}\right) - \frac{a\tau\,\Delta\omega}{\Delta T^2(\beta^2+a^2)}\right], \end{aligned} \tag{4}$$

with

$$\begin{aligned} \theta(\Delta\omega) = & \frac{a\Delta\omega^2}{4}\left(\frac{1}{\beta^2+a^2} - \frac{1}{\gamma}\right) - \frac{\Delta\omega\,\tau\beta}{\Delta T^2(\beta^2+a^2)} - \frac{a\tau^2}{\Delta T^4(\beta^2+a^2)} \\ & + \frac{1}{2}\arctan\left(a T_c^2\right) - \frac{3}{2}\arctan(a/\beta), \end{aligned} \tag{5}$$

where $\Delta\omega = \omega_0 - \omega$, $\beta = T_c^{-2} + \Delta T^{-2}$, and $\gamma = T_c^{-4} + a^2$. Here the quadratic term of k is neglected on the assumption that the modulation coefficient is very small and $k\,E_{THz} << b$. We confirmed that the waveform obtained from Eq. (4) agrees with that from Eq. (3) through the numerical integration of $I(\omega)\_on$ and $I(\omega)\_off$ with the same parameter values.

2.3. Experiment

A schematic diagram of the experimental setup for EODCP is illustrated in **Figure 3**. A regeneratively amplified femtosecond laser beam with a temporal width of ~150 fs (FWHM), a wavelength of 800 nm, a repetition rate of ~1 kHz, and a pulse energy of ~600 μJ was divided into two beams: one was irradiated onto an InAs (1 0 0) wafer to generate the terahertz field pulse and the other was chirped by passing it through a pair of gratings. We used two types of grating pairs, i.e., 1200 and 600 grooves/mm, to change the chirp rate. All the measurements in the present study were made in the atmosphere.

We employed a double-beam configuration to obtain $I(\omega)\_on$ and $I(\omega)\_off$ simultaneously. This configuration reduces the effect of the shot-to-shot fluctuation of the laser on the EODCP-derived terahertz waveform. The chirped beam was first passed through a polarizer and then divided into two beams. One beam, the reference $R(\omega)$ was led into a fiber that transferred the light to a spectrometer and was detected with a charge-coupled device (CCD) image sensor. The other, the signal $S(\omega)$ was aligned to travel collinearly with the terahertz field pulse, modulated by the terahertz field within a 1-mm-thick ZnTe crystal and was passed through an analyzer into the other fiber. The reference and signal beams were detected simultaneously on two different areas of the image sensor. $S(\omega)\_off$ and $R(\omega)\_off$ were measured simultaneously in the absence of the terahertz field, while $R(\omega)\_on$ and $S(\omega)\_on$ (= $I(\omega)\_on$) were measured in the presence of it. $I(\omega)\_off$ was obtained by $R(\omega)\_on \times S(\omega)\_off/R(\omega)\_off$. Thus, we could measure $I(\omega)\_off$ and $I(\omega)\_on$ simultaneously in the double-beam configuration and derive the terahertz field waveform using Eq. (3). Moreover, an optical delay line (delay line 1 in **Figure 3**) was employed in order to vary the time difference between the chirped probe pulse and the terahertz field pulse within the EO crystal. This was necessary to obtain the value of the chirp rate experimentally.

Figure 4 shows $I(\omega)\_on$ (black) and $I(\omega)\_off$ (red) obtained from a single-shot measurement at a chirp rate of −0.24 THz^2, together with the terahertz waveform derived from Eq. (3) (blue). The figure demonstrates that the modulation due to the terahertz field obviously appears in $I(\omega)\_on$ even for the single-shot measurement. However, the signal-to-noise ratio is roughly 10:1 and not so high. Further, the baseline is distorted and not zero. Thus, in the present study, the data were acquired by averaging over a few hundred shots to achieve a good signal-to-noise ratio.

2.4. Dependence of the terahertz field waveform on the chirp rate

Figure 5(a) displays the EODCP-derived terahertz waveform at a chirp rate of −0.24 THz^2. The waveform is shifted along the abscissa (wavelength) when the delay time between the chirped probe and terahertz field pulses is changed. **Figure 5(b)** was obtained by tracking corresponding peak positions (arrow in **Figure 5(a)**) in the terahertz waveforms at different delay times. We derived the value of the chirp rate from the slope of the line fitted to the data points. It was found that this value agrees with that obtained by a second-harmonic-generation frequency-resolved optical grating (SHG-FROG) measurement and the value estimated from the distance between the two gratings and the number of grooves ruled on the grating per unit length. The upper axis in **Figure 5(a)** is the time axis obtained from the wavelength

http://dx.doi.org/10.5772/67195

axis using the chirp rate value. The temporal width of the chirped pulse at this chirp rate was determined to be ~15 ps (FWHM) by cross-correlation measurement between the original femtosecond pulse and the chirped one.

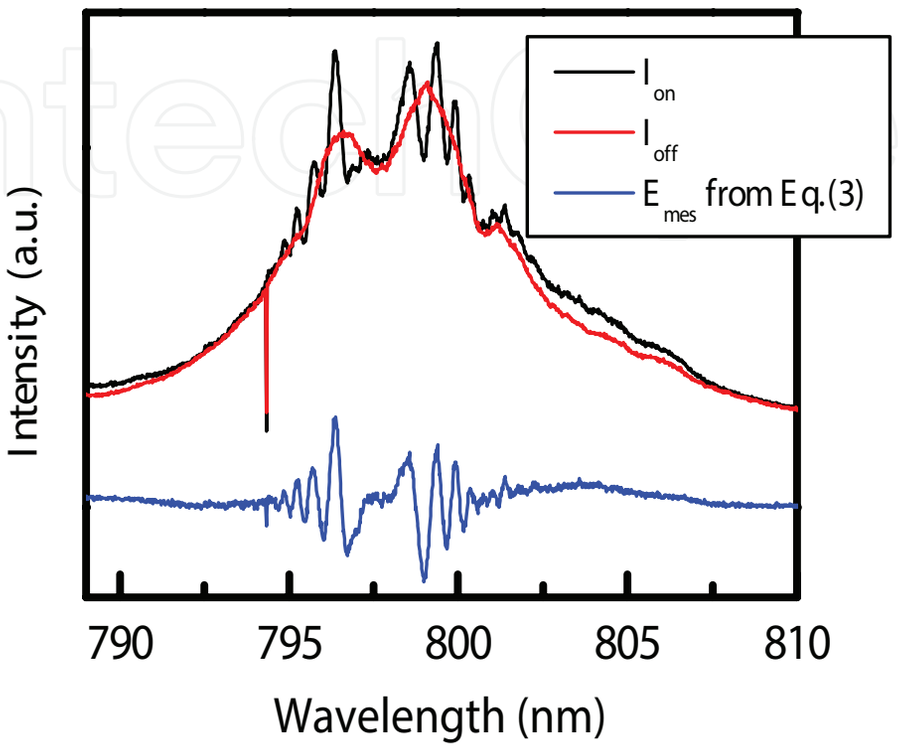

Figure 4. Chirped probe pulses with terahertz field modulation ($I(\omega)\_on$) and without it ($I(\omega)\_off$) obtained from a single-shot EODCP measurement, i.e., with no data accumulation; a negative spike at around 794 nm is due to the damage of the sensor element. The terahertz waveform derived from Eq. (3) is drawn by a blue line.

The EODCP-derived terahertz waveforms (blue line:−0.24 THz^2, red line:−1.9 THz^2) are compared with that obtained by THz-TDS with delay scanning (black line) in **Figure 5(c)**. We note that the temporal observation window becomes narrower with decreasing the chirp rate, and hence, it is a part of the full-time range in the figure for the chirp rate of −1.9 THz^2. The waveform due to the THz-TDS with delay scanning is monocyclic, although small long-lived oscillation due to absorption by water vapor in the terahertz frequency range is involved. Meanwhile, the waveforms measured by EODCP are multicyclic; the cycle number is considerably large at −0.24 THz^2, compared with at −1.9 THz^2. Such multicyclic behavior was not observed in the terahertz field waveform obtained using EODCP by Jiang and Zhang [9], although the temporal width of the chirped probe pulse in their measurement is comparable to that in the case of −0.24 THz^2. Further, it should be noted that the temporal period of the muticycle in the EODCP-derived terahertz waveform is roughly the same as that of the monocycle obtained by THz-TDS with delay scanning in **Figure 5(c)**, whereas the former was three times longer than the latter in the measurement by Jiang and Zhang [9]. This implies that the temporal resolution of EODCP is comparable to that of THz-TDS with delay scanning in our case.

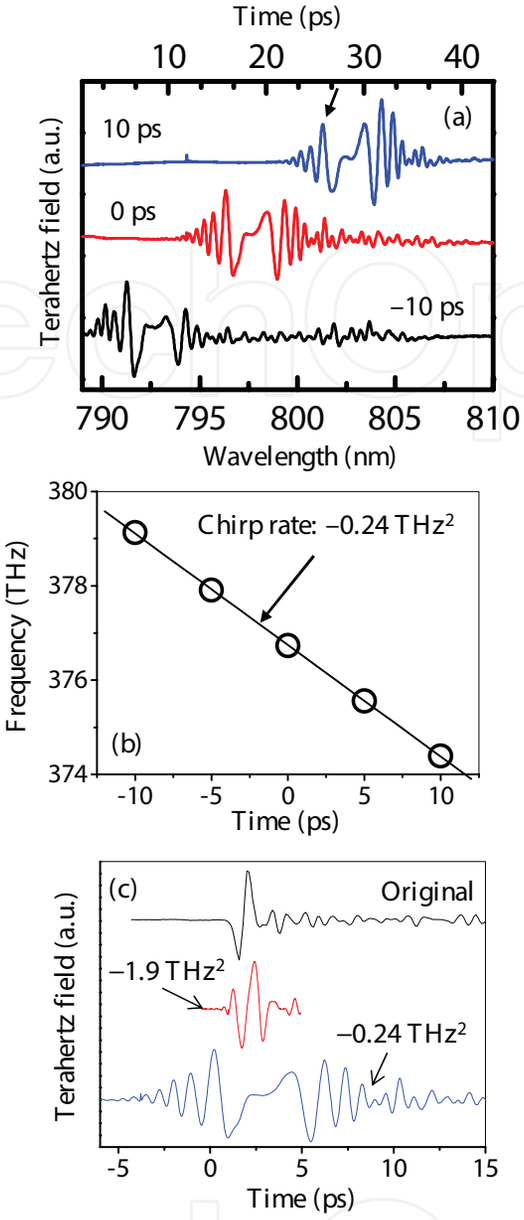

Figure 5. (a) The terahertz waveforms obtained by EODCP with a chirp rate of −0.24 THz² at three delay times between the input terahertz field and chirped probe pulses. The ordinate of each waveform is shifted for the sake of clarity. (b) Corresponding peak positions (arrow in (a)) in the terahertz waveform, represented by frequency, plotted as a function of the delay time (circles). The chirp rate is obtained from the slope of the solid line fitted to the data. The upper abscissa in Figure (a) is derived from the lower one using the chirp rate value. (c) The EODCP-derived terahertz waveforms (blue line:−0.24 THz², red line:−1.9 THz²) are compared with that obtained by THz-TDS with delay scanning using a unchirped probe pulse (black line). The ordinate of each waveform is shifted for the sake of clarity. Reproduced from Murakami et al. J. Appl. Phys. **104**, 103111 (2008), with the permission of AIP Publishing.

The terahertz waveforms calculated from Eq. (4) at [a (THz²), T_c (ps)] = (−0.12, 22), (−0.65, 4), and (−1.5, 1.8), with τ = 0 ps, ΔT = 0.45 ps, and ω_0 = 375 THz (=800 nm) are illustrated in **Figure 6**, together with the original terahertz field pulse (inset) used for the calculation; here we note that the time step corresponding to the wavelength one depends on the chirp rate and that the time step becomes smaller with decreasing the chirp rate. The waveform is found to

http://dx.doi.org/10.5772/67195

change from monocyclic to multicyclic behavior with decreasing the magnitude of chirp rate. This tendency agrees with that seen in the experimental result of **Figure 5(c)**. It should be noted that the multicyclic behavior does not emerge in the waveform derived on the assumption that the stationary phase method is valid, as shown by Sun and coworkers [10]. Hence, the analysis based on the stationary phase method is not applicable to the case where the EODCP-derived terahertz waveform is multicyclic.

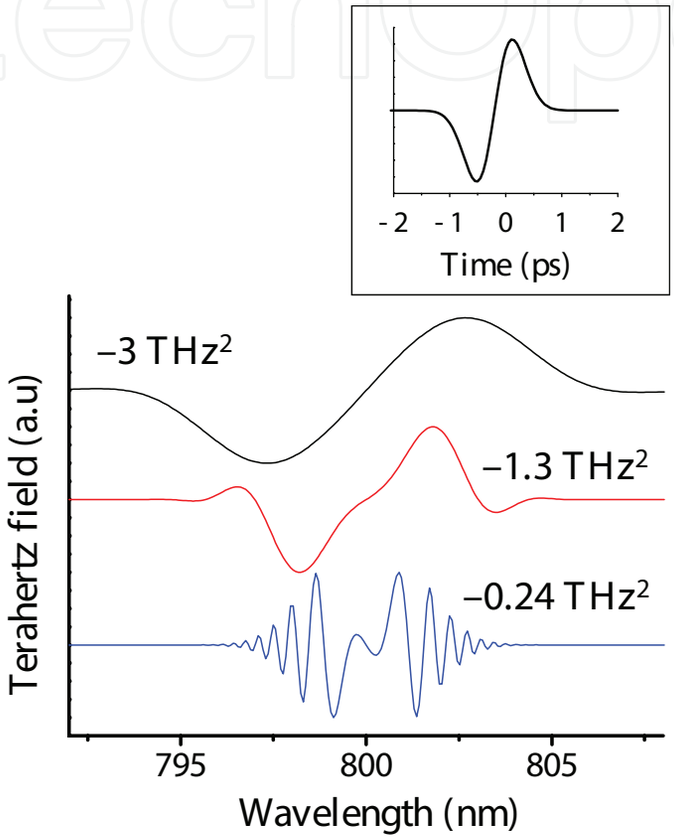

Figure 6. Chirp rate dependence of the terahertz waveform calculated from Eq. (4), where [a (THz^2), T_c (ps)] = (−0.12, 22), (−0.65, 4) and (−1.5, 1.8). The chirp rate value is given by 2a. The ordinate of each waveform is shifted for the sake of clarity. We note that the time step corresponding to the wavelength one depends on the chirp rate, and that the time step becomes smaller with decreasing the chirp rate. The inset shows the original terahertz waveform used for the calculation. Reproduced from Murakami et al. J. Appl. Phys. **104**, 103111 (2008), with the permission of AIP Publishing.

2.5. Dependence of the EODCP-derived terahertz waveform on spectral resolution of the spectrometer

Figure 7 shows the dependence of the EODCP-derived terahertz waveform on the spectral resolution of the spectrometer at a chirp rate of −1.9 THz^2. The waveform does not exhibit monocyclic behavior at the high spectral resolution (0.2 nm, FWHM), whereas it becomes monocyclic and temporally broadened at the low resolution (3 nm). Therefore, it is found that the spectral resolution of the spectrometer plays an important role in determining the terahertz waveform obtained by EODCP.

The terahertz waveform measured by Jiang and Zhang does not show multicyclic features despite the fact that the chirp rate and temporal width of the chirped probe pulse are comparable to those in our case at −0.24 THz^2. This may be because the spectral resolution of the spectrometer used by them was not high enough to resolve the multicyclic waveform, although its value is not described in the literature [9].

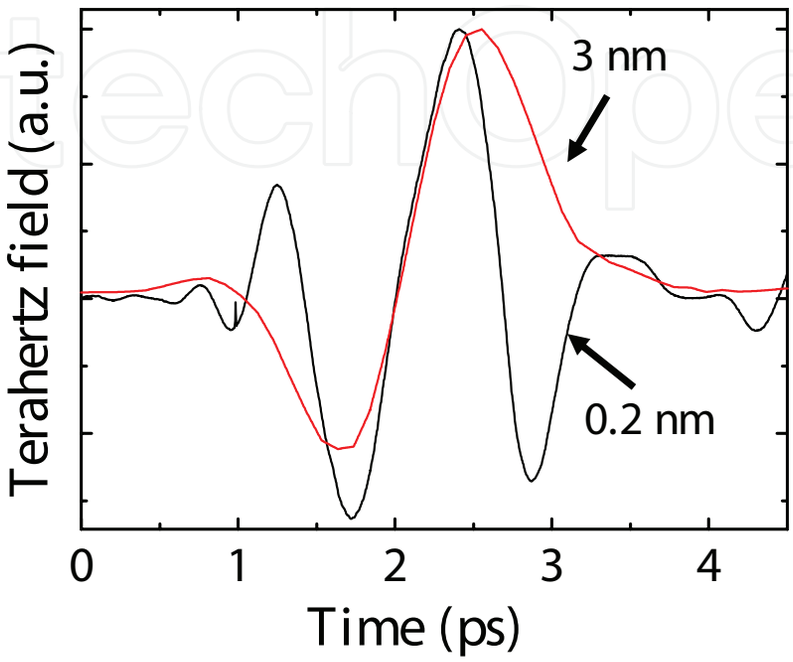

Figure 7. Terahertz waveforms measured by EODCP at two spectral resolutions of the spectrometer (0.2 nm (black line) and 3 nm (red line))at a chirp rate of −1.9 THz^2. Reproduced from Murakami et al. J. Appl. Phys. **104**, 103111 (2008), with the permission of AIP Publishing.

2.6. Terahertz spectroscopy using EODCP

In order to attain high spectral resolution in THz-TDS, the terahertz waveform needs to be measured in a given temporal observation window, according to time-frequency relation based on the Fourier transform. A time window of a few tens of picoseconds is required to obtain spectral resolution as small as 1 cm^{-1} (30 GHz). EODCP with a small chirp rate leads to a narrow temporal observation window under the limited spectral width of the probe pulse (~10 nm in the present study), as seen in **Figure 5(c)**, and so a high spectral resolution is not achieved. Therefore, EODCP with a small chirp rate has a crucial drawback for terahertz spectroscopy, even if the terahertz waveform approaches the original one. Thus, we have to use a chirped probe pulse with a chirp rate that assures an observation window of a few tens of picoseconds, although we will encounter multicyclic behavior in the terahertz waveform in such a case.

The multicyclic behavior in the terahertz waveform calculated from Eq. (4) at a chirp rate of −0.24 THz^2 leads to the oscillating behavior in the frequency spectrum, as shown in **Figure 8**; although the envelope connecting the peaks in the spectrum coincides with the spectrum obtained from the Fourier transform of the original terahertz field waveform (inset of **Figure 6**). Thus, we consider the effect of the oscillating behavior on the derivation of the

http://dx.doi.org/10.5772/67195

optical constant of materials by terahertz spectroscopy using EODCP. The quadratic term of the modulation coefficient is neglected in the derivation of Eq. (4), which implies that the EODCP instrument exhibits a linear response to the terahertz field. Under the condition of such a linear response, the EODCP-derived terahertz waveform is expressed by

$$E_{ref}(t) = \int_0^\infty \varphi(t - t_1)\, E_0(t_1) dt_1, \tag{6}$$

where $\varphi(t)$ and $E_0(t)$ are the time profile of the instrumental response and the original terahertz field, respectively. If the terahertz field is transmitted through a material under examination and measured by EODCP, its waveform is given by

$$E_{sig}(t) = \iint \varphi(t - t_1)\eta(t_1 - t_2)\, E_0(t_2) dt_1\, dt_2, \tag{7}$$

where the material is assumed to exhibit a linear response to the terahertz field and the response function is denoted by $\eta(t)$. Thus, the complex transmission coefficient $\tilde{\eta}(\omega)$ of the material is derived by

$$\tilde{\eta}(\omega) = \frac{\tilde{E}_{sig}(\omega)}{\tilde{E}_{ref}(\omega)} \tag{8}$$

with

$$\tilde{E}_{sig}(\omega) = \tilde{\varphi}(\omega)\tilde{\eta}(\omega)\, \tilde{E}_0(\omega) \quad \text{and} \quad \tilde{E}_{ref}(\omega) = \tilde{\varphi}(\omega)\, \tilde{E}_0(\omega), \tag{9}$$

where the terms with a tilde, e.g.,$\tilde{E}_{sig}(\omega)$, are the Fourier transforms of the corresponding terms without a tilde, e.g., $E_{sig}(t)$. The convolution theorem is used in the derivation of Eq. (9). The Fourier-transformed spectra of the instrument response function and the original terahertz waveform are canceled out in Eq. (8), and so have no effect on derivation of the optical constant of the material. The complex refractive index is derived from the complex transmission coefficient [47].

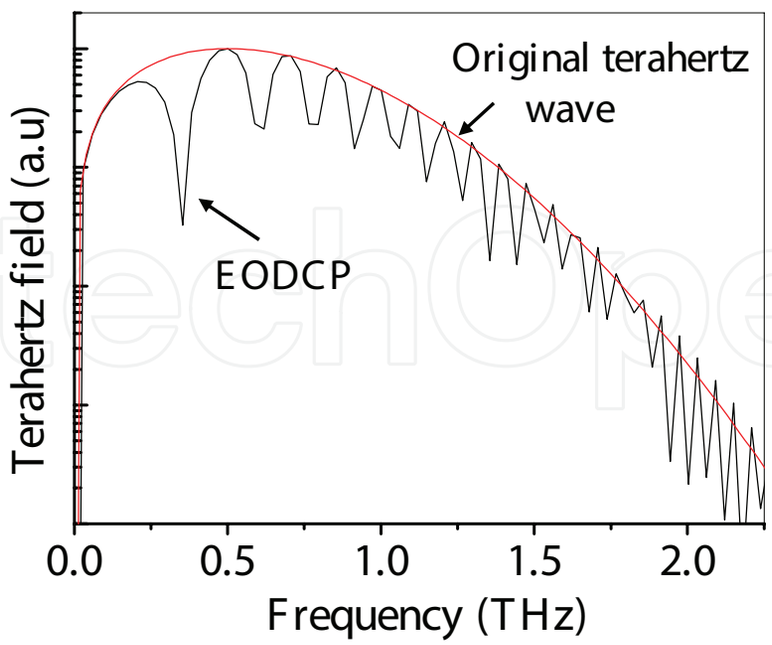

Figure 8. Frequency spectra obtained from the Fourier transform of the terahertz waveform calculated from Eq. (4) at a chirp rate of −0.24 THz^2 (black line) and the original waveform (red line). A logarithmic scale is used for the ordinate. Reproduced from Murakami et al. J. Appl. Phys. **104**, 103111 (2008), with the permission of AIP Publishing.

The EODCP-derived terahertz waveform depends on the delay time between the terahertz field and chirped probe pulses, as shown in **Figure 5(a)**. This implies that the instrument response of EODCP varies with the delay time. If the refractive index of a material examined is not unity in the terahertz spectral range, the terahertz field pulse transmitted through the material is delayed from that passing through free space by an amount determined by the refractive index. And thus, the two terahertz field pulses modulate temporally different portions of the chirped probe pulse. Therefore, the instrument response is different for the two terahertz fields. A method to remove the effect of variable instrument response is to make the two terahertz field pulses overlap with the same (temporal) portion of the chirped probe pulse using an optical delay line, although the time difference between the two terahertz field pulses must be measured in advance. The chirped probe beam can be modulated by the terahertz field at any temporal portion using the optical delay line (delay line 1 in **Figure 3**).

In order to examine the applicability of terahertz spectroscopy using EODCP, we measured the optical constant of a material by the method and compared the result with that by THz-TDS with delay scanning. A semi-insulating GaAs crystal (1 0 0) with a thickness of 500 μm was used as a sample. **Figure 9(a)** illustrates the terahertz waveforms observed using EODCP in the presence (red line) and absence (black line) of GaAs, where the optical delay line (delay line 1 in **Figure 3**) was not changed for the two measurements, i.e., we did not adjust the temporal overlapping between the chirped and terahertz field pulses. Both the waveforms exhibit multicycle behavior owing to the small magnitude of the chirp rate. The terahertz wave transmitted through the GaAs substrate changes its waveform and is delayed compared with the wave in the absence of the GaAs substrate. We derive the complex refractive index $\tilde{n}(\omega) = n(\omega) - i\kappa(\omega)$ of the material with a thickness of d from the following equation using the complex amplitude spectra obtained from the Fourier transform of the two terahertz waveforms,

$$\frac{E_{sig}(\omega)}{E_{ref}(\omega)} = \tilde{t}_{as}(\omega)\exp\left\{-i\frac{(\tilde{n}(\omega)-1)d\omega}{c}\right\}\left[\sum_{l=1}^{m}\left\{(\tilde{r}_{sa}(\omega))^2\exp\left(-i\frac{2\tilde{n}(\omega)d\omega}{c}\right)\right\}^l\right]\tilde{t}_{sa}(\omega), \quad (10)$$

$$\tilde{t}_{as}(\omega) = \frac{2}{\tilde{n}(\omega)+1},\ \tilde{r}_{sa}(\omega) = \frac{\tilde{n}(\omega)-1}{\tilde{n}(\omega)+1},\ \tilde{t}_{sa}(\omega) = \frac{2\tilde{n}(\omega)}{\tilde{n}(\omega)+1},$$

where $\tilde{t}_{as}(\omega)$ and $\tilde{t}_{sa}(\omega)$ are a complex Fresnel coefficient for transmission at the sample surface, and a subscript of "as" or "sa" indicates that the terahertz wave proceeds into the sample or out of it. Further, $\tilde{r}_{sa}(\omega)$ is a complex Fresnel coefficient for reflection at the sample surface, where multireflection at the sample surface is taken into account. We use a successive approximation method for the numerical calculation. The complex refractive index thus derived is compared with that due to THz-TDS with delay scanning in **Figure 9(b)**. The agreement between the two results is good, and so the multicyclic profile of the terahertz waves obtained using EODCP does not affect derivation of the optical constant in this case.

A preliminary application of OPTP spectroscopy using EODCP was conducted for the same GaAs. The experimental system is schematically described in **Figure 3**. A second harmonic femtosecond pulse (~400 nm) generated with a BBO crystal was used as a pump light to produce charge carriers. The terahertz wave is reflected by the charge carriers, and so one can measure the lifetime of the charge carrier by time-resolved terahertz reflection or transmission spectroscopy. **Figure 10(a)** is the terahertz waveform after transmission through the GaAs substrate as a function of delay time between the optical pump and terahertz probe pulses using optical delay

http://dx.doi.org/10.5772/67195

line 2 in **Figure 3**. The time-dependent change in the terahertz waveform is seen in **Figure 10(a)**. From the peak amplitudes of the frequency spectra, the time profile of the normalized reflectivity is derived, as plotted by circles in **Figure 10(b)**. On the other hand, OPTP spectroscopy using terahertz waveform measurements with delay scanning is applicable for GaAs, because the initial state is recovered in the period of the laser pulse repetition (~1 ms). From the peak amplitude of the terahertz waveform, the time-resolved normalized reflectivity was derived, as shown by a red line in **Figure 10(b)**. The results due to the two methods agree with each other and show a single exponential decay with a time constant of ~1 ns. Thus, it is demonstrated that terahertz waveform measurements using EODCP are a promising method for OPTP spectroscopy.

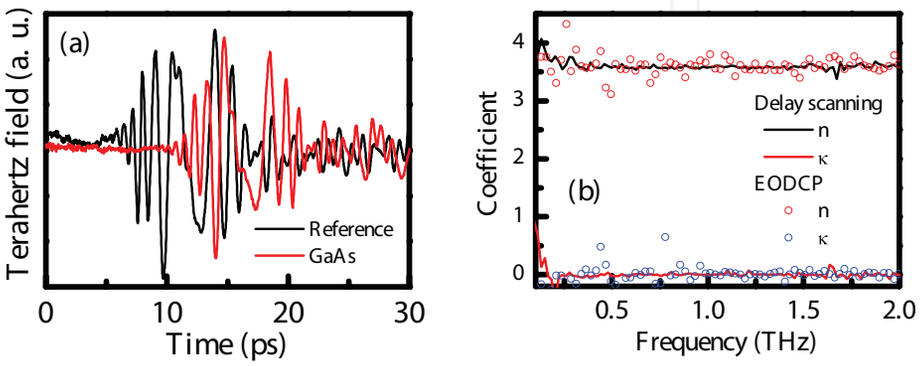

Figure 9. (a) Waveforms of the terahertz field pulses transmitted through a 0.5-mm-thick GaAs substrate (red line) and in the absence of the sample (black line), observed using EODCP. (b) The complex refractive index $\tilde{n}(\omega) = n(\omega) - i\kappa(\omega)$ of the sample derived from Eq. (10) using the complex amplitude spectrum obtained from the Fourier transform of the two terahertz waveforms in Figure (a) (circles), together with the result due to the terahertz waveforms measured by THz-TDS with delay scanning (lines).

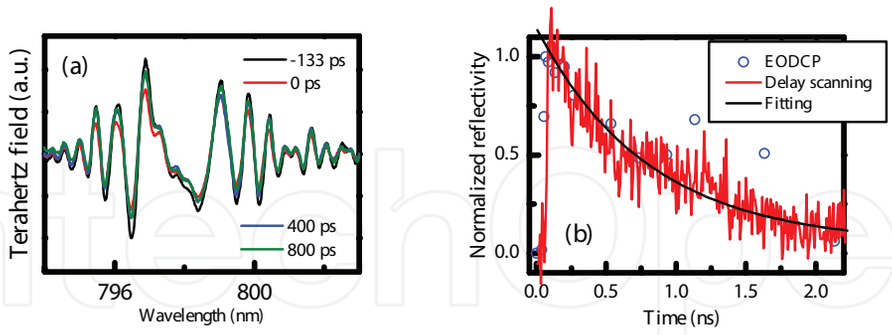

Figure 10. (a) Terahertz waveforms after transmission through the GaAs substrate measured by OPTP spectroscopy with EODCP at several pump-probe delay times. (b) The time-dependent normalized reflectivity (circles) derived from the peak amplitudes of the frequency spectra obtained from the Fourier transform of the terahertz waveforms, together with the result due to OPTP spectroscopy using THz-TDS with delay scanning (red line) and exponential decay curve with a time constant of ~1 ns (black line).

2.7. Future studies

Future work necessary for the development of the EODCP method is as follows. (1) We need to make the signal-to-noise ratio high for the single-shot measurement. One way for it is to use a

detector with a wide dynamic range, for example, high-charge capacity to low readout noise in CCDs. The laser intensity is high enough to attain high signal-to-noise ratio. However, practically it is too strong for any sensors, and so the input intensity is usually much attenuated to prevent the sensor from saturation. (2) More pulse-to-pulse stability in the laser beam spot, polarization, and so on, in the femtosecond laser is required for the single-shot measurement. We used the double-beam configuration for the measurement, and so the pulse-to-pulse fluctuation in the laser frequency spectrum was corrected. However, the baseline of the terahertz waveform derived was distorted in the single-shot measurement (**Figure 4**). This implies that the laser fluctuation other than the spectral fluctuation affects the measurement. (3) It is interesting to perform the EODCP measurement using a chirped probe pulse with a wide spectral width and large magnitude of the chirp rate. In the present study, we used a chirped pulse with a small magnitude of it for the application of terahertz spectroscopy because of the narrow spectral width of the laser (~10 nm). There is a Ti:sapphire femtosecond laser whose spectral width is several tens of nanometers. It allows us to conduct EODCP measurements in a wide temporal observation window even by use of a chirped pulse with large magnitude of the chirp rate. As the magnitude of the chirp rate is raised, the EODCP-derived terahertz waveform approaches a monocyclic behavior, and correspondingly, the spectrum in the frequency domain shows less oscillating behavior. Thus, EODCP with such a chirped pulse will be advantageous for terahertz spectroscopy.

3. Experiment of THz-TDS of reverse micellar solution

Before describing the results of terahertz spectroscopy of the reverse micellar solutions, the experimental procedures are described in this section.

3.1. Sample

Myoglobin, AOT [=*bis*(2-ethyl-hexyl)sulfosuccinate], isooctane, and millipore water were used as a protein, surfactant, oil, and water, respectively, for preparation of the PCR micellar solutions. AOT was dried in a vacuum oven at 45°C. A Karl Fisher titrator was used to measure the water content in the samples. Two methods were applied for preparation of the PCR micellar solution. One is the so-called "injection method," i.e., a small amount of protein aqueous solution was injected into AOT/isooctane solution, and the other is a paste method, proposed by us; the two methods are described in detail elsewhere [48]. The reverse micellar solution (without a protein) was prepared by the injection method of a small amount of water.

3.2. Sample cell

A sample cell has an optical path length of 1 cm and two sample-chambers with the same dimension (dual cell); one is for a sample signal, and the other is for a reference signal, as seen in **Figure 1**. In the measurement of PCR micellar solution (Section 4), we used the PCR micellar solution for a sample signal and oil solvent for a reference signal. On the other hand, in the temperature-dependent THz-TDS of water in the reverse micellar solution (Section 5), we used reverse micellar solutions with water for a sample signal and without water for a reference signal. The dual cell is fixed on a computer-controlled stage, and the measurement of the two

http://dx.doi.org/10.5772/67195

samples was iteratively made by moving the stage for accumulation of the data. The measurement using the dual cell decreases the distortion of the absorption spectrum due to long-period fluctuation of the laser, in comparison with the measurement using a single cell, because the time interval between the measurements of the two samples is short, typically one minute.

3.3. Derivation of the optical constant in the measurement using a dual cell

We used THz-TDS with delay scanning for the reverse micellar solutions. The absorption coefficient $\alpha(\omega)$ and refractive index $n(\omega)$ of a sample were derived as follows: (1) the waveforms of the terahertz fields transmitted through the two solutions were converted to frequency-domain data (i.e., the intensity: $I_s(\omega)$ and $I_r(\omega)$, phase: $\phi_s(\omega)$ and $\phi_r(\omega)$; s : sample, and r : reference) using Fourier transform, (2) the absorption coefficient was derived from $\alpha(\omega) = d^{-1} ln [I_r(\omega)/I_s(\omega)]$, where d is the optical path length of the cell (1 cm in the present study), (3) the refractive index was derived with the equation $n_s(\omega) - n_r(\omega) = c(\omega d)^{-1}(\phi_s(\omega) - \phi_r(\omega))$, where $n_s(\omega)$ and $n_r(\omega)$ are the refractive indices of the sample and reference solutions, respectively, and c is the speed of light. A spherical reverse micelle is formed owing to the self-assembly of AOT molecules even if there is almost no water in the solution [49]. In the measurement of water in the reverse micellar solution (Section 5), the two solutions in the dual cell had the same concentration of AOT. Therefore, we assumed that the contribution of AOT molecules to the optical constant is canceled out in their derivation [50]. On the other hand, the absorption and phase shift of the terahertz wave by isooctane is very small because of its nonpolar nature, and so the effect of isooctane on the optical constant was considered negligible.

3.4. Absorption lineshape function

The absorption lineshape function $\tilde{C}(\omega)$ is given by

$$\tilde{C}(\omega) = \frac{A\alpha(\omega)n(\omega)}{\omega\left[1 - \exp\left(-\frac{\hbar\omega}{k_B T}\right)\right]} \tag{11}$$

$$= \frac{1}{2\pi}\int_{-\infty}^{+\infty} dt\, e^{-i\omega t} C(t), \tag{12}$$

$$C(t) = \langle M(0) \cdot M(t) \rangle \tag{13}$$

where $A = 3c\hbar(2\pi)^{-2}$, $\hbar$ is the reduced Planck constant, k_B is the Boltzmann constant, and T is the sample temperature [51, 52]. Eq. (11) indicates that the lineshape function is expressed by the Fourier transform of the time-correlation function $C(t)$ of the total dipole moment $M(t)$ of the system examined. The absorption lineshape function was calculated from Eq. (11) by use of the absorption coefficient and refractive index obtained from the measurements with THz-TDS, and then the relaxation process was examined using the correlation function.

3.5. Cryostat for temperature-dependent measurements

It is necessary that the reference and sample solutions are at the same temperature to obtain the correct optical constant of the sample at a given temperature. Therefore, the dual cell was fixed in a custom-made stainless-steel cryostat, and its temperature was controlled within approximately ±1 K using nitrogen gas flow from a liquid nitrogen vessel. The waveforms of the terahertz fields transmitted through the two solutions were alternately measured using a computer-controlled stage on which the cryostat was fixed.

We examined the baselines of the absorption coefficient and refractive index obtained from the THz-TDS using the temperature-controlled dual cell. To that end, the sample and reference cells were filled with the same AOT reverse micellar solution, and the temperature-dependent measurement of THz-TDS was made in the 273–296 K temperature range. The results are depicted in **Figure 11**, together with the optical constant of water in the reverse micellar solution with w_0 = 35 at 295 K. **Figure 11(a)** demonstrates that all the baselines of the absorption coefficient are flat in the frequency range between 0.1 and 1.2 THz; here, the standard deviation of the mean is around 6×10^{-3}. As for the refractive index, the baselines are flat and approximately unity, shifted only by ~3×10^{-3}, with the standard deviation of the mean of ~2×10^{-5} in **Figure 11(b)** in the same frequency range. The standard errors are small enough compared with the values of the optical constants, and hence, the experimental system used works for temperature-dependent measurements of the optical constant. Thus, we analyzed the optical constant in this terahertz frequency range.

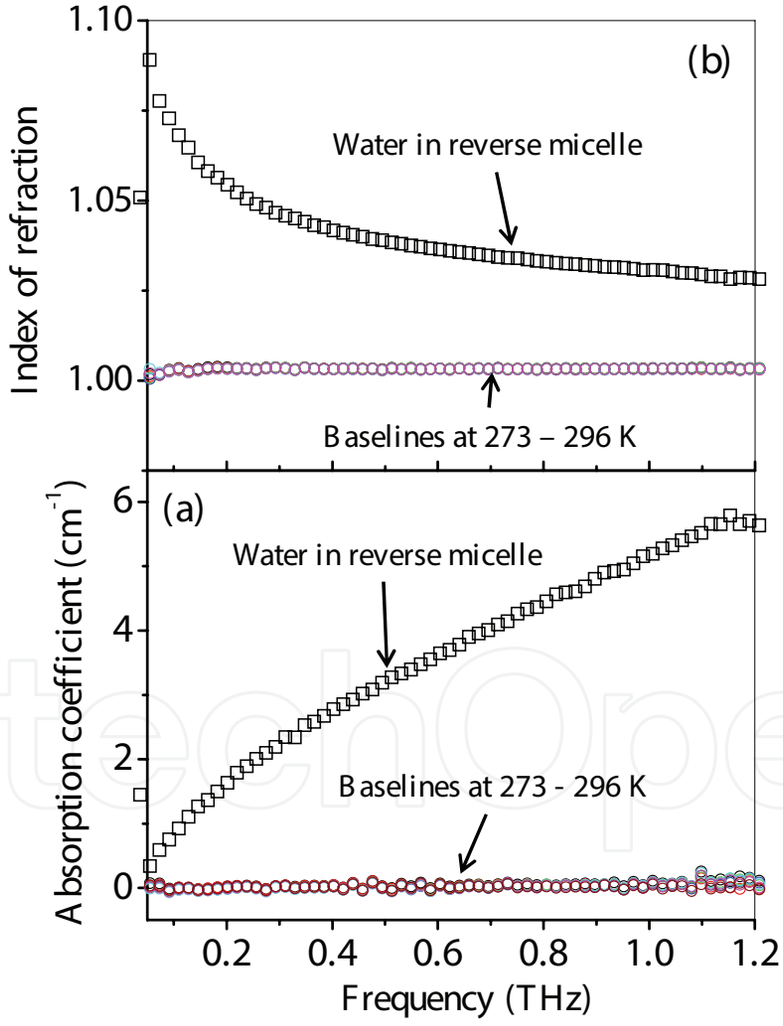

Figure 11. Temperature dependence of baselines for (a) the absorption coefficient and (b) the refractive index measured by THz-TDS with delay scanning using a temperature-controlled dual cell. The sample and reference cells were filled with the same AOT reverse micellar solution. The baselines at 273, 278, 283, 287, 293, and 296 K are shown by circles, and the optical constants of water in the AOT reverse micelle at w_0 = 35 and 295 K by squares. Adapted from Murakami et al. (2015), with permission of Elsevier.

4. Terahertz spectroscopy of PCR micellar solution

4.1. Protein concentration dependence of the absorption spectra

The protein concentration dependence of the absorption spectra of the PCR micellar solution at w_0 = 4.4 and 0.2 is displayed in **Figure 12(a)** and **(b)**, respectively. The amplitude of the spectrum becomes large with the raising of the protein concentration at w_0 = 0.2 in the spectral range examined, whereas it decreases at w_0 = 4.4. This is understood by the fact that the amplitude of the absorption spectrum of hydration water is smaller than that of bulk water in the terahertz spectral range [44, 53], as described below. Here we note that PCR micellar solution is a binary system of PCR micelles and protein-unfilled, i.e., water-containing reverse (WCR) micelles, because it is difficult that protein molecules are introduced into all the reverse micelles in the solution. The molar ratio of bulk-like to interfacial-hydrated water within the WCR micelle increases with increasing w_0 value [54–59]. The number of water molecules in the WCR micelle is estimated to be ~5 at w_0 = 0.2 and ~250 at w_0 = 4.4, whereas in the PCR micelle, it is estimated to be ~20 at w_0 = 0.2 and ~580 at w_0 = 4.4 [24, 48]. Moreover, the number of AOT molecules in the WCR micelle is estimated to be ~20 at w_0 = 0.2 and ~60 at w_0 = 4.4, whereas in the PCR micelle, it is estimated to be 110 at w_0 = 0.2 and ~130 at w_0 = 4.4 [24, 48]. Hence, almost all the water molecules within the WCR micelle will be bound to AOT molecules at w_0 = 0.2, whereas some of water molecules are bulk-like at w_0 = 4.4; we note that one AOT molecule has at least a few hydration sites [54]. In the PCR micelle, almost all the water molecules will be bound to the protein or AOT molecule at the two w_0 values; the first hydration shell of myoglobin includes several hundred water molecules [60]. Therefore, the bulk-like water becomes hydration one in the PCR micellar solution at w_0 = 4.4, when the WCR micelle disappears by formation of the PCR micelle. Thus, if the decrease in the amplitude of the absorption spectrum owing to hydration exceeds the increase due to the protein, the total spectral amplitude descends with increasing the protein concentration at w_0 = 4.4. On the other hand, the spectral amplitude increases by the contribution of protein with raising the protein concentration at w_0 = 0.2, because all the water molecules in both the WCR and PCR micelles are hydration water at w_0 = 0.2. Although there could be a difference between the spectra of hydration waters bound to AOT and protein, the effect of the difference is not observed in the abovementioned result of protein concentration dependence.

4.2. Derivation of terahertz absorption spectrum of a protein in a reverse micelle

We analyze the absorption spectra by

$$\alpha(\omega) = C_P \varepsilon_{\text{protein}}(\omega) + C_{\text{water}} \varepsilon_{\text{water}}(\omega) + C_S \varepsilon_S(\omega), \tag{14}$$

where $\varepsilon_{\text{protein}}(\omega)$, $\varepsilon_{\text{water}}(\omega)$, and $\varepsilon_S(\omega)$ are the molar extinction coefficients of protein, water, and surfactant in the PCR micellar solution, respectively, and C_P, C_{water} and C_S are the molar concentrations of protein, water, and surfactant, respectively. We do not take account of the effect of the interactions between the different constituents on the spectrum in Eq. (12). Moreover, the contribution of a low content of water will be negligible at w_0 = 0.2. On the other hand, the surfactant molecules are aggregated to form reverse micelles with and without a protein.

Therefore, we assume that the molar extinction coefficient of the surfactant in the PCR micellar solution is independent of the protein concentration. On these assumptions, we obtain the molar extinction coefficient of the protein from the difference spectrum between the absorption spectra at two protein concentrations, i.e.,

$$\Delta\alpha(\omega) = \left(C_P' - C_P\right)\varepsilon_{\text{protein}}(\omega) = \Delta C_P\,\varepsilon_{\text{protein}}(\omega)$$
$$\varepsilon_{\text{protein}}(\omega) = \Delta\alpha(\omega)/\Delta C_P \quad . \tag{15}$$

The molar extinction coefficient of the protein thus derived is depicted in **Figure 12(c)**, where combinations of the protein concentration for the difference spectrum are 1.5–0.72 mM (circles), and 1.5–0.34 mM (squares). The two spectra agree with each other in **Figure 12(c)**, and so the assumptions made above are considered to be valid. Thus, the terahertz absorption spectrum of the protein in the reverse micelle is derived from the protein concentration dependence of the absorption spectrum of the PCR micellar solution.

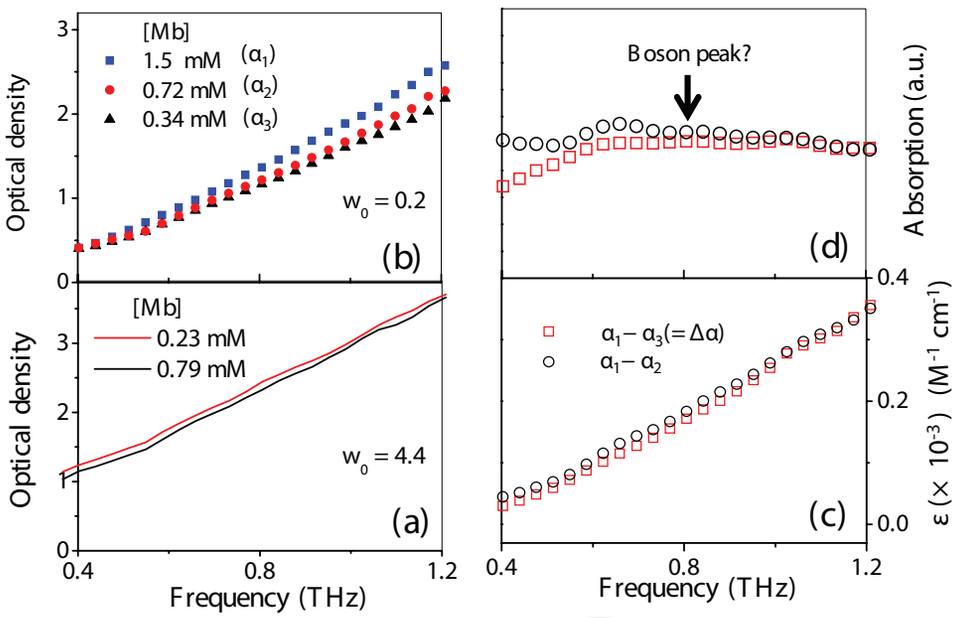

Figure 12. (a) Protein concentration dependence of the absorption spectra of the PCR micellar solution at w_0 = 4.4 and (b) w_0 = 0.2 at room temperature. (c) Molar extinction coefficient of myoglobin within the PCR micelle derived from the difference spectrum between the absorption spectra at different protein concentrations at w_0 = 0.2. (d) Absorption lineshape function of myoglobin obtained from Eq. (11). Adapted from Murakami et al. (2012), with permission of Elsevier.

4.3. Future studies

The terahertz spectrum in **Figure 12(c)** has no characteristic peaks, as seen for protein powder and liquid samples. This is considered to be so because a protein molecule has a large number of low frequency modes [61, 62] and shows structural fluctuations [63, 64]. The detailed interpretation of the terahertz spectrum of protein molecules is a future problem. Finally, this terahertz spectrum of myoglobin in relation to the boson peak of protein is discussed. It is well known from inelastic neutron and Raman scattering measurements of proteins that proteins show a broad spectrum with a peak position at around 1 THz, which is called the boson peak

http://dx.doi.org/10.5772/67195

[65–67]. The origin of the boson peak has not been completely understood. Further, the boson peak is observed not only for proteins but also for a wide range of glassy materials such as polymers and glass-forming liquids. The molar extinction coefficient is proportional to frequency and includes a Bose-Einstein factor. In order to compare the result of terahertz spectroscopy with those of inelastic neutron and Raman-scattering measurements, the absorption lineshape function must be derived by removing such frequency dependence, as described in Section 3.4, where we assume that the frequency dependence of the refractive index is negligible in this limited frequency range. **Figure 12(d)** is the absorption lineshape function thus derived. It is found that the spectrum shows a broad peak at around 0.8 THz, which is identical with that from inelastic neutron-scattering measurements of hydrated myoglobin [65]. An interesting thing is that this peak is observed at room temperature because the boson peak of proteins is observed below ~200 K in the inelastic neutron-scattering measurement. Thus, the broad peak observed in the PCR micellar solution could be a new candidate to clarify the mechanism of the boson peak, and further investigation will be performed and reported elsewhere.

5. Temperature-dependent terahertz spectroscopy of water in reverse micellar solutions

The Stokes radius of the reverse micelle examined ($w_0 = 35$) was ~12 nm at room temperature. It was found from temperature-dependent dynamic light-scattering measurements that this reverse micelle shows the water shedding at 286 K (**Figure 14(a)**) [45].

5.1. Spectral analysis

We analyzed the absorption lineshape function obtained from Eq. (11). The refractive index of water in the reverse micellar solution exhibits almost no frequency-dependent change in the frequency range examined and is close to unity, as seen in **Figure 11(b)**. Consequently, the refractive index does not affect the frequency dependence of the absorption lineshape function. Thus, we calculate $\tilde{C}(\omega)$ at $n(\omega) = 1$.

For curve fitting the absorption lineshape function, a sum of two exponential relaxations with time constants of τ_f for a fast component and τ_s for a slow one was employed for $C(t)$, i.e., $C(t) = A_f e^{-t/\tau_f} + A_s e^{-t/\tau_s}$, where A_f and A_s are the amplitudes for the fast and slow components, respectively. This leads to the sum of the two Lorentzian functions in the frequency domain by Eq. (12), i.e.,

$$F(\omega) = 2A_f\tau_f^{-1}\left(\omega^2 + \tau_f^{-2}\right)^{-1} + 2A_s\tau_s^{-1}\left(\omega^2 + \tau_s^{-2}\right)^{-1} + B. \quad (16)$$

This model can be regarded as the Debye model with two relaxation times [41–43, 52]. A term of B in Eq. (16) is a constant baseline necessary for a better fit. Water shows an ultrafast Debye relaxation of ~0.1 ps [41–43, 52], and its contribution to the absorption lineshape function is considered to be a constant baseline because the upper limit of the frequency range examined is too low to analyze the spectral shape due to the ultrafast relaxation. The fitting procedure using a nonlinear least squares method was identical for the absorption lineshape functions at all the temperatures examined.

The curve fitting using Eq. (16) does well for the absorption lineshape function of water in the reverse micelle solution at all the temperatures examined, as displayed in **Figure 13**. The fitting curve (black line) agrees well with the curve obtained from the experiment (circles), where the curves due to the fast component (blue line), the slow component (red line), and the baseline (green line) are also depicted. Thus, the time constants of the fast and slow components are acquired from the fitting. There is a question regarding the uniqueness of the time constants derived from the curve fitting, although multi-parameter fitting is a common method for spectral analysis [41–43, 68, 69]; in fact, as shown for liquid water in **Figure 14(c)**, there is a small difference between the time constants from the two literatures [41, 42, 68]. However, a systematic deviation due to the fitting procedure should not influence the conclusion on the basis of the temperature dependence of the values derived from the same procedure.

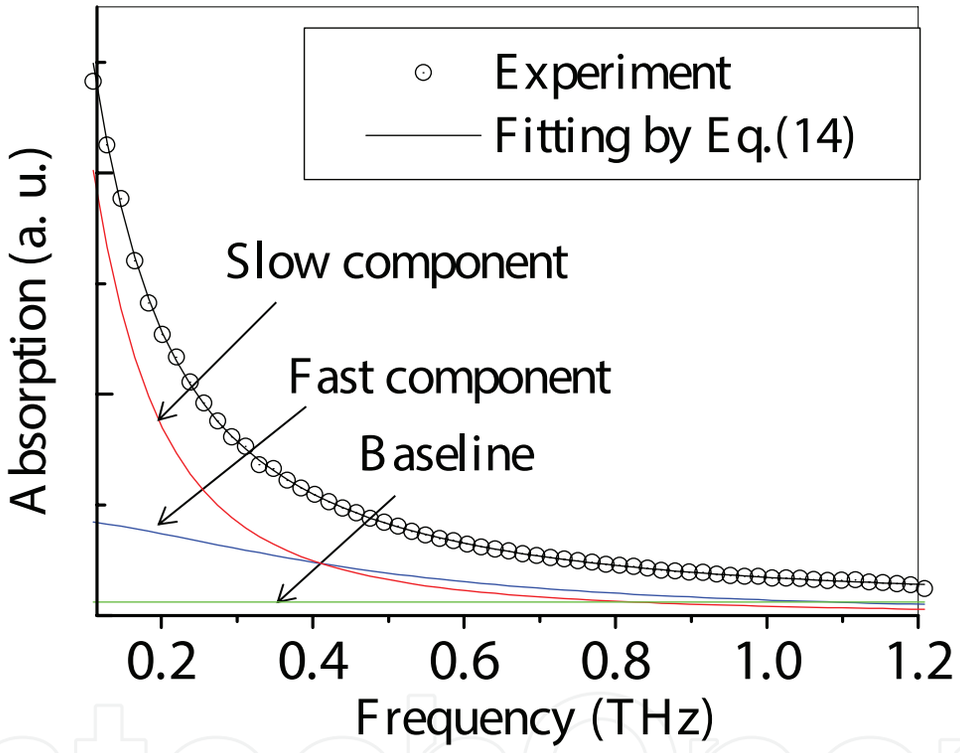

Figure 13. A result of the curve fitting using Eq. (16) of the absorption lineshape function obtained from Eq. (11) at 295 K. The contributions of the fast (blue) and slow (red) components and constant baseline (green) in Eq. (16) to the fitting curve are also illustrated. Reproduced from Murakami et al. (2015), with permission of Elsevier.

5.2. Temperature dependence of the relaxation time

Figure 14(b) shows the waveforms of the terahertz field pulses transmitted through the two solutions at 286 K (=T_c). Eight sets of data are superimposed in the figure. All the waveforms are reproduced for the reference solution, whereas the waveform for the sample solution abruptly changes during the repeated measurement. Since T_c is identical to the temperature at which the water shedding occurs in the reverse micellar solution, the change in the waveform for the sample solution is attributed to the water shedding.

http://dx.doi.org/10.5772/67195

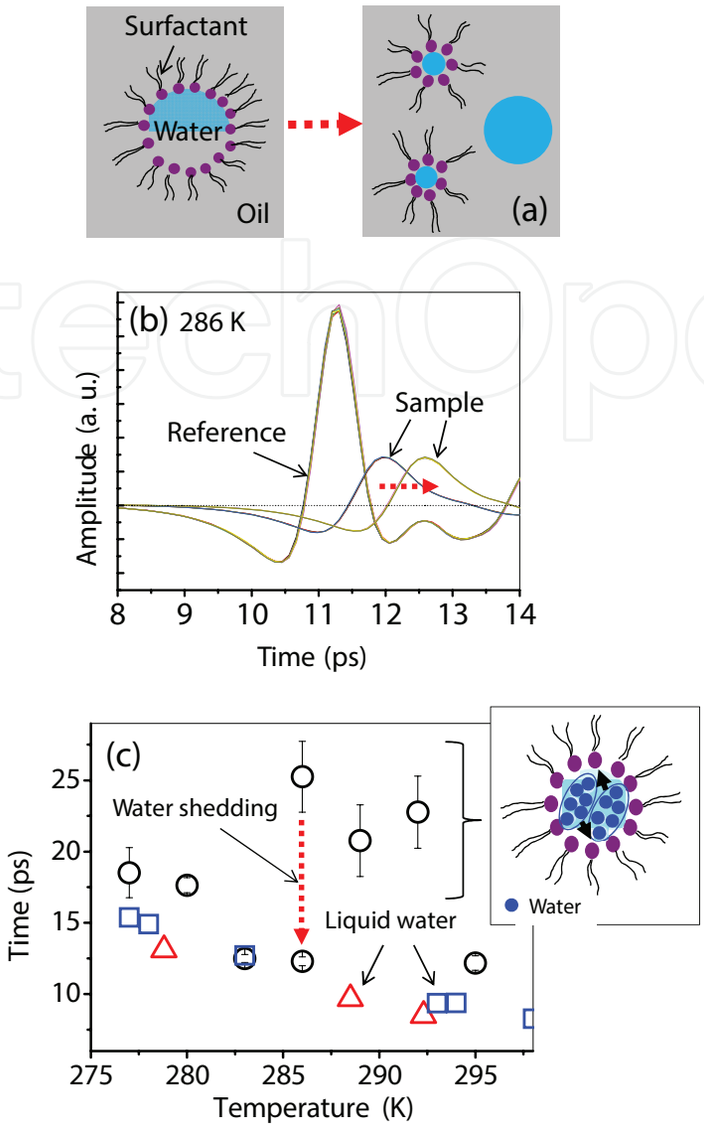

Figure 14. (a) Schematic cross-section of a reverse micelle before (left) and after the water shedding (right). (b) The terahertz waveforms after transmission through the sample and reference solutions at 286 K. Data obtained by THz-TDS (delay scanning) measurements repeated eight times are superimposed. The reference solution is AOT/isooctane solution without water, whereas the sample solution is that with water at $w_0 = 35$. The waveform for the sample solution changes (red arrowed dashed line) during the repeated measurement. (c) The time constant of the slow component obtained by the curve fitting using Eq. (16), together with the data of liquid water from literature [41, 42] (triangles) and [68] (squares). An abrupt drop (red arrowed dashed line) in the time constant occurs during the repeated measurement at 286 K. The inset shows that the confinement of the reverse micelles affects the collective motions of water with a cooperative length comparable with the aqueous cavity length. Adapted from Murakami et al. (2015), with permission of Elsevier.

The temperature dependence of the time constant of the slow component (circles) is depicted in **Figure 14(c)**, together with the results for liquid water (triangles [41, 42] and squares [68]) from literature. There are three characteristic findings as the temperature is reduced. First, considerable slowing down occurs above T_c compared with the case of liquid water. Second, the time constant dramatically decreases at T_c (red arrowed dashed line); this corresponds to a change in the terahertz waveform of the sample solution at T_c, as seen in **Figure 14(b)**.

Lastly, the temperature-dependent behavior of the time constant is similar to that of liquid water below T_c. On the other hand, the time constant of the fast component was found to be in the range from ~2 ps to 4 ps, and an abrupt drop in the time constant is observed at T_c [45].

5.3. Relaxation process before and after the water shedding

The slow component is due to the collective motions of water molecules observed in THz-TDS of liquid water. This is reasonable because almost all the water molecules in the reverse micelle are bulk-like at $w_0 = 35$. THz-TDS measurements of liquid water demonstrated that the relaxation time exhibits a power-law temperature dependence as $(T - T_s)^{-1}$) ($T_s = 228$ K) above the melting point of water [41, 42]. The power-law temperature dependence implies that the cooperative nature of the water motion becomes large with reducing temperature, i.e., a larger hydrogen-bond network is formed for the motion at lower temperatures; accordingly, the time scale of the water motion increases. Such a mechanism is valid for water confined in large reverse micelles. However, the confinement of the reverse micelles should affect the mechanism, as illustrated in the inset of **Figure 14(c)**, and hence, it is reasonable that the slowing down of the relaxation process with decreasing temperature is enhanced in the reverse micelle compared with that in liquid water.

A dramatic drop in the time constant at T_c in **Figure 14(c)** is due to water shedding from the reverse micelle. The expelled water is free from the confinement of the reverse micelle. Therefore, the relaxation process of the water will speed up compared with that of the water within the reverse micelle. Moreover, it is reasonable that the relaxation process of the expelled water is similar to that of liquid water below T_c, as seen in **Figure 14(c)**. We have recently shown for a reverse micelle containing a water-soluble probe molecule that the diffusion-like motion of the water molecules surrounding the probe molecule becomes active upon the water and dye molecule shedding from the reverse micelle [36]. This is a kind of speeding up of the water motion induced by the water shedding.

5.4. Future studies

The present study demonstrates that there is a distinct difference between the properties of water in and out of the cage, and that water extracted from the reverse micelle exhibits the relaxation process similar to that of liquid water. Therefore, the water droplet free from the cage is expected to be more appropriate for studies of the properties of supercooled water at low temperatures than water confined in the cage. The results on temperature-dependent THz-TDS of water in smaller reverse micelles that show the water-shedding below the melting point of water will be reported elsewhere.

6. Concluding remarks

Protein-containing reverse micelles are suitable systems for terahertz spectroscopy of protein molecules in liquid. Moreover, terahertz waveform measurements using EODCP is a promising

method for OPTP spectroscopy. The next step is OPTP spectroscopy of PCR micellar solution. As seen in **Figure 12(b)**, the optical density of the protein molecule is very small in the terahertz range even for its high concentration, which is practically attained. Therefore, it will be necessary that the protein molecule exhibits large spectral change involved in the photoreaction induced by the pump optical pulse, where high quantum efficiency is needed for the photoreaction. If a protein exhibits a narrow band peak at the frequency characteristic of the collective motion coupled with the reaction, we expect to observe distinct change in the time-resolved terahertz spectrum. Further, it is noted that we used PCR micelles with a few tens of water molecules (w_0 = 0.2) to obtain the absorption spectrum of the protein molecule. On the other hand, at w_0 = 4.4, the spectrum of the protein molecule is buried in the large spectral contribution of ~600 water molecules around the protein one. A certain number of water molecules, with which the first hydration shell will be at least filled, will be required for the biological reaction of protein molecules. Hence, the water content in the reverse micelle has to be adjusted to the minimum under the condition that the biological reaction of protein occurs. Here, the hydration water is considered to contribute to the characteristic change in the time-resolved terahertz spectrum because it should move in concert with the protein's motion.

Acknowledgements

The author thanks M. Katsurada, K. Shimizu, Y. Toyota, T. Nishi, and S. Nashima for their collaboration. These studies were partly supported by Grants-in-Aid for Scientific Research (23654139 and 22310038).

Author details

Hiroshi Murakami

Address all correspondence to: murakami.hiroshi@qst.go.jp

National Institutes for Quantum and Radiological Science and Technology (QST), Kizuga City, Kyoto, Japan

References

[1] Y. -S. Lee, *Principles of terahertz science and technology* (New York, Springer, 2009).

[2] *Terahertz frequency detection and identification of materials and objects*, edited by R. E. Miles, X. -C. Zhang, H. Eisele, and A. Krotkus (Springer, Dordrecht, 2007).

[3] K. Y. Kim, B. Yellampalle, J. H. Glownia, A. J. Taylor, and G. Rodriguez, Phys. Rev. Lett. **100**, 135002 (2008).

[4] S. Kar, D. R. Mohapatra, E. Freysz, and A. K. Sood, Phys. Rev. B **90**, 165420 (2014).

[5] P. D. Cunningham and L. M. Hayden, J. Phys. Chem. C **112**, 7928 (2008).

[6] J. R. Danielson, Y. -S. Lee, J. P. Prineas, J. T. Steiner, M. Kira, and S. W. Koch, Phys. Rev. Lett. **99**, 237401 (2007).

[7] M. Jewariya, M. Nagai, and K. Tanaka, Phys. Rev. Lett. **105**, 203003 (2010).

[8] M. C. Hoffmann, J. Hebling, H. Y. Hwang, K. -L. Yeh, and K. A. Nelson, J. Opt. Soc. Am. B **26**, 29 (2009).

[9] Z. Jiang and X. -C. Zhang, Appl. Phys. Lett. **72**, 1945 (1998).

[10] F. G. Sun, Z. Jiang, and X. -C. Zhang, Appl. Phys. Lett. **73**, 2233 (1998).

[11] H. Murakami, K. Shimizu, M. Katsurada, and S. Nashima, J. Appl. Phys. **104**, 103111 (2008).

[12] D. A. Turton, H. M. Senn, T. Harwood, A. J. Lapthorn, E. M. Ellis, and K. Wynne, Nat. Commun. **5**, 3999 (2014).

[13] S. Hay and N. S. Scrutton, Nat. Chem. **4**:161 (2012).

[14] K. Itoh and M. Sasai, Proc. Natl. Acad. Sci. USA **101**, 14736 (2004).

[15] F. G. Parak, Rep. Prog. Phys. **66**, 103 (2003).

[16] E. Castro-Camus and M. B. Johnston, Chem. Phys. Lett. **455**, 289 (2008).

[17] S. E. Whitmire, D. Wolpert, A. G. Markelz, J. R. Hillebrecht, J. Galan, and R. R. Birge, Biophys. J. **85**, 1269 (2003).

[18] J. Xu, K. W. Plaxco, and S. J. Allen, J. Phys. Chem. B **110**, 24255 (2006).

[19] C. Zhang and S. M. Durbin, J. Phys. Chem. B **110**, 23607 (2006).

[20] S. Ebbinghaus, S. J. Kim, M. Heyden, X. Yu, U. Heugen, M. Gruebele, D. M. Leitner, M. Havenith, Proc. Natl. Acad. Sci. USA **104**, 20749 (2007).

[21] S. Ebbinghaus, S. J. Kim, M. Heyden, X. Yu, M. Gruebele, D. M. Leitner, and M. Havenith, J. Am. Chem. Soc. **130**, 2374 (2008).

[22] *Reverse micelles*, edited by P. L. Luisi, and B. E. Straub (Plenum Press, New York, 1984).

[23] *Structure and reactivity in reverse micelles*, edited by M. P. Pileni (Elsevier, Amsterdam, 1989).

[24] H. Murakami, Y. Toyota, T. Nishi, and S. Nashima, Chem. Phys. Lett. **519–520**, 105 (2012).

[25] B. van den Berg, R. Wain, C. M. Dobson, R. J. Ellis, EMBO J. **19**, 3870 (2000).

[26] C. Wichmann, P. T. Naumann, O. Spangenberg, M. Konrad, F. Mayer, and M. Hoppert, Biochem. Biophys. Res. Commun. **310**, 1104–1110 (2003).

[27] *Water: The forgotten biological molecule*, edited by D. L. Bihan and H. Fukuyama, (Pan Stanford, Singapore, 2011).

[28] S. K. Pal, J. Peon, B. Bagchi, and A. H. Zewail, J. Phys. Chem. B **106**, 12376 (2002).

[29] C. A. Angell, Ann. Rev. Phys. Chem. **34**, 593 (1983); in *Water : A Comprehensive treatise*, edited by F. Franks (Plenum, New York, 1982) Vol. 7, p. 1.

[30] O. Mishima and H. E. Stanley, Nature **396**, 329 (1998).

[31] H. E. Stanley, S. V. Buldyrev, P. Kumar, F. Mallamace, M. G. Mazza, K. Stokely, L. Xu, and G. Franzese, J. Non-cryst. Solids **357**, 629 (2011).

[32] L. Liu, S. -H. Chen, A. Faraone, C. -W. Yen, and C. -Y. Mou, Phys. Rev. Lett. **95**, 117802 (2005).

[33] P. Gallo, M. Rovere, and S. -H. Chen, J. Phys. Chem. Lett. **1,** 729 (2010).

[34] J. Hedström, J. Swenson, R. Bergman, H. Jansson, and S. Kittaka, Eur. Phys. J. Special Topics **141**, 53 (2007).

[35] K. Yoshida, T. Yamaguchi, S. Kittaka, M. -C. Bellissent-Funel, and P. Fouquet, J. Phys.: Condens. Matter **24,** 064101 (2012).

[36] H. Murakami, T. Sada, M. Yamada, and M. Harada, Phys. Rev. E **88**, 052304 (2013).

[37] C. Boned, J. Peyrelasse, and M. Moha-Ouchane, J. Phys. Chem. **90**, 634 (1986).

[38] A. K. Simorellis, W. D. V. Horn, and P. F. Flynn, J. Am. Chem. Soc. **128**, 5082 (2006).

[39] T. Spehr, B. Frick, I. Grillo, P. Falus, M. Müller, and B. Stühn, Phys. Rev. E **79**, 031404 (2009).

[40] C. A. Munson, G. A. Baker, S. N. Baker, and F. V. Bright, Langmuir, **20**, 1551 (2004).

[41] C. Rønne, P. -O. Åstrand, and S. R. Keiding, Phys. Rev. Lett. **82**, 2888 (1999).

[42] C. Rønne and S. R. Keiding, J. Mol. Liq. **101 (1–3)**, 199 (2002).

[43] J. T. Kindt and C. A. Schmuttenmaer, J. Phys. Chem. **100**, 10373 (1996).

[44] T. Arikawa, M. Nagai, and K. Tanaka, Chem. Phys. Lett. **457**, 12 (2008).

[45] H. Murakami, J. Mol. Liq. **210**, 37 (2015).

[46] B. Yellampalle, K. Y. Kim, G. Rodriguez, J. H. Glownia, and A. J. Taylor, Opt Exp. **15**, 1376 (2007).

[47] L. Duvillaret, F. Garet, and J. L. Coutaz, IEEE J. Sel. Top. Quantum Electron **2**, 739 (1996).

[48] H. Murakami, T. Nishi, and Y. Toyota, J. Phys. Chem. B **115**, 5877 (2011).

[49] M. Kotlarchyk, J. S. Huang, and S. -H. Chen, J. Phys. Chem. **89**, 4382 (1985).

[50] D. M. Mittleman, M. C. Nuss, and V. L. Colvin, Chem. Phys. Lett. **275**, 332 (1997).

[51] R. G. Gordon, Adv. Mag. Reson. **3**, 1 (1968).

[52] S. R. Keiding, J. Phys. Chem. A **101**, 5250 (1997).

[53] S. Mashimo, S. Kuwabara, S. Yagihara, K. Higasi, J. Phys. Chem. **91**, 6337 (1987).

[54] G. Onori, A. Santucci, J. Phys. Chem. **97**, 5430 (1993).

[55] D. E. Moilanen, E. E. Fenn, D. Wong, M. D. Fayer, J. Phys. Chem. B **113**, 8560 (2009).

[56] D. Cringus, A. Bakulin, J. Lindner, P. Vöhringer, M. S. Pshenichnikov, D. A. Wiersma, J. Phys. Chem. B **111**, 14193 (2007).

[57] A. M. Dokter, S. Woutersen, H. J. Bakker, Phys. Rev. Lett. **94**, 178301 (2005).

[58] P. Dutta, P. Sen, S. Mukherjee, A. Halder, K. Bhattacharyya, J. Phys. Chem. B **107**, 10815 (2003).

[59] R. E. Riter, D. M. Willard, N. E. Levinger, J. Phys. Chem. B **102**, 2705 (1998).

[60] I. D. Kuntz, J. Am. Chem. Soc. **93**, 514 (1971).

[61] B. K. Rai, E. W. Prohofsky, and S. M. Durbin, J. Phys. Chem. B **109**, 18983 (2005).

[62] A. Kitao, F. Hirata, N. Go, Chem. Phys. **158**, 447 (1991).

[63] A. Ansari, J. Berendzen, S. F. Bowne, H. Frauenfelder, I. E. T. Iben, T. B. Sauke, E. Shyamsunder, and R. D. Young, Proc. Natl. Acad. Sci. USA. **82**, 5000 (1985).

[64] K. Gunasekaran, B. Ma, and R. Nussinov, Proteins: Structure, Func.Bioinform. **57**, 433 (2004).

[65] S. Cusack and W. Doster, Biophys. J. **58**, 243 (1990).

[66] Y. Joti, A. Kitao, and N. Go, J. Am. Chem. Soc. **127**, 8705 (2005).

[67] P. Kumar, K. T. Wkfeldt, D. Schlesinger, L. G. M. Pettersson, and H. E. Stanley, Sci. Rep. **3**, 1980 (2013).

[68] U. Kaatze and V. Uhlendorf, Z. Phys. Chem. Neue Folge, **126**, 151 (1981).

[69] J. Barthel, K. Bachhuber, R. Buchner, and H. Hetzenauer, Chem. Phys. Lett. **165**, 369 (1990).